

See discussions, stats, and author profiles for this publication at: <https://www.researchgate.net/publication/363215693>

The spatial-temporal patterns of East Asian climate in response to insolation, CO₂ and ice sheets during MIS-5

Article in *Quaternary Science Reviews* · October 2022

DOI: 10.1016/j.quascirev.2022.107689

CITATIONS

2

READS

169

2 authors:



Anqi Lyu

Nansen Environmental and Remote Sensing Center

13 PUBLICATIONS 109 CITATIONS

[SEE PROFILE](#)



Qiuzhen Yin

Université Catholique de Louvain - UCLouvain

99 PUBLICATIONS 3,039 CITATIONS

[SEE PROFILE](#)

Some of the authors of this publication are also working on these related projects:



WarmClim [View project](#)



The spatial-temporal patterns of East Asian climate in response to insolation, CO₂ and ice sheets during MIS-5

Anqi Lyu ^a, Qiuzhen Yin ^{a,*}

^a Georges Lemaitre Center for Earth and Climate Research, Earth and Life Institute, Université Catholique de Louvain, 1348 Louvain-la-Neuve, Belgium



ARTICLE INFO

Article history:

Received 30 April 2022

Received in revised form

12 July 2022

Accepted 27 July 2022

Available online xxx

Handling Editor: Dr Yan Zhao

Keywords:

Interglacial

MIS-5

East Asian summer monsoon

Astronomical parameters

Ice sheets

CO₂

ABSTRACT

Marine Isotope Stage (MIS) 5, between about 130 and 70 ka BP, is characterized by climate oscillations consisting of three interstadials and two stadials. Many climate simulations have been performed for the warmest MIS-5e period, but few has been made to cover the entire MIS-5 to investigate the climate variability during this long period. In this study, two sets of snapshot simulations by a step of 2 ka covering the whole MIS-5 period are performed with the model HadCM3 to investigate the relative impacts of insolation, CO₂ and Northern Hemisphere ice sheets on the East Asian climate variability. Our results show that precipitation and temperature in different subregions in East Asia have different sensitivity to astronomical forcing, CO₂ and ice sheets, in particular when seasonal and mean annual changes are concerned. The variability of temperature and precipitation within MIS-5 is mainly controlled by precession but their magnitudes are modulated by CO₂ and ice sheets. The impact of ice sheets on summer precipitation vary between subregions and is sensitive to ice sheet configurations and background insolation. The summer precipitation in southern China is more sensitive to ice sheets than in northern China. Moisture budget analysis show that insolation and CO₂ affect the summer precipitation by the dynamic and thermodynamic processes, respectively, and the impact of ice sheets is mainly through the vertical dynamic processes which is strongly associated with the ice sheet-induced wave train at the hemisphere scale.

© 2022 The Authors. Published by Elsevier Ltd. This is an open access article under the CC BY-NC-ND license (<http://creativecommons.org/licenses/by-nc-nd/4.0/>).

1. Introduction

Marine Isotope Stage (MIS) 5, lasting from ~130 to ~70 thousand years before present (ka BP), is a relatively long MIS according to marine δ¹⁸O records (Imbrie et al., 1984), but it is characterized by large climate oscillations which include three warm interstadials (MIS-5a, 5c and 5e) and two relatively cool stadials (MIS-5b and 5d). The interstadial MIS-5e, which is often referred as the last interglacial (LIG), is one of the warmest interglacials in many paleoclimate records. For example, the global mean annual surface temperature during MIS-5e was suggested to be 2 °C higher than the Pre-Industry (PI) and slightly higher than today, with more pronounced warming in the North Hemisphere (NH), especially at high latitudes (CAPE-Last Interglacial Project Members, 2006; Clark and Huybers, 2009; Masson-Delmotte et al., 2013; Capron et al., 2014). As a result, MIS-5e has been a focus for data syntheses (Landais et al., 2016) and climate modeling (Herold et al., 2012;

Nikolova et al., 2013; Otto-Bliesner et al., 2013; Yin et al., 2021). However, climate simulations for the other periods of MIS-5 are rare and therefore the mechanisms of climate variations during the entire MIS-5 are less understood.

Numerous paleoclimate reconstructions show that MIS-5 is characterized not only by a warm climate in many regions but also by intensified East Asia monsoon. The climate variations during MIS-5 over East Asia have been reconstructed by using various natural archives, such as marine and lacustrine sediments, ice cores, loess records, and cave speleothems (e.g. Yao et al., 1997; Cheng et al., 2016; Wang et al., 2016). Many reconstructions show that the East Asian summer monsoon (EASM) is stronger, and the climate is warmer and wetter during MIS-5 than during Pre-Industrial. However, there are huge discrepancies in time and space, and the mechanisms responsible for these discrepancies are still unclear. For example, Hu et al. (2015) indicated the asynchronous responses of speleothem growth rates during MIS-5 in East China and Northwest China. Jia et al. (2016) suggested that late MIS-5e was the wettest period in western CLP based on loess records, while Xue et al. (2019) showed that early MIS-5e was the wettest

* Corresponding author.

E-mail address: qiuzhen.yin@uclouvain.be (Q. Yin).

based on speleothem records.

Model simulations have been performed to investigate how the EASM responds to astronomical forcing during MIS-5. However, most studies focus on MIS-5e, and research on other time slices is limited. Snapshot simulations for MIS-5e and -5c of Shi et al. (2018) show that intensified EASM leads to less precipitation in East China and more precipitation in further north. A transient simulation using the model CCSM3 and an acceleration factor of 100 which covers the last 150 ka shows an in-phase relationship between the NH mid-latitude summer insolation and the simulated annual precipitation in East Asia, dominated by the 20 ka precessional cycle (Li et al., 2013). All these studies targeting on the EASM focused on the effect of the astronomical forcing. However, it should be noted that ice sheets and CO₂ could also have important effects on the regional climate in East Asia (Yin et al., 2009; Shi et al., 2020), in particular when the whole period of MIS-5 is considered, because non-negligible ice sheets existed in the NH during most part of MIS-5 (~4–29 million km³) and CO₂ had large variations (~213–277 ppmv). The influence of ice sheets on temperature arises from both thermodynamic and dynamic effects. The largest temperature anomalies usually occur in the areas covered by ice sheets, with very strong cooling due to the high albedo (thermodynamic effect). At the same time ice sheets could also remotely change temperature in the EASM region and surrounding oceans by changing the upper atmospheric circulation related to their height (dynamic effect) (Ullman et al., 2014; Cao et al., 2019). The oceanic processes, for example, Atlantic Meridional Overturning Circulation and El Niño–Southern Oscillation, can further influence temperature in East Asia (Lu et al., 2016). The processes make the response of temperature to ice sheet distribution non-linear, especially at mid-latitudes (Gao et al., 2020). Modelling studies show that the influence of ice sheets on the EASM precipitation is also non-linear and depends on the background insolation and the size, shape, location of ice sheets (Yin et al., 2008, 2009).

In order to have a complete understanding of the climate variations during MIS-5, simulations which cover the entire period of MIS-5 and consider not only the astronomical forcing but also the variations of CO₂ and ice sheets, are performed in this study with the model HadCM3. We intend to understand the spatial and temporal variations of the East Asian climate during MIS-5 and the relative effects of insolation, CO₂ and ice sheets. This paper is organized as follows. Section 2 describes the model, experiments setup and analysis methods. In Section 3, we explore the influence of astronomical parameters and CO₂ on temperature and precipitation during MIS-5. In Section 4, the simulated climate changes with different configurations of ice sheets are compared. In Section 5, we evaluate the simulated climate during MIS-5 and the related uncertainties. Conclusions are given in Section 6.

2. Methods

2.1. Model

HadCM3 (Hadley Centre Coupled Model, version 3) is a fully coupled AOGCM (atmosphere-ocean coupled general circulation model), which was developed in the U.K. Met Office Hadley Center for Climate Prediction and Research. The atmospheric component in HadCM3 is a global grid-point hydrostatic primitive equation model. It has 19 hybrid levels in the vertical direction, with a 2.5° × 3.75° horizontal resolution and 96 × 73 grid cells (Pope et al., 2000). The spatial resolution over the ocean component is 1.25° × 1.25° (288 × 73 grid cells) with 20 vertical layers (Gordon et al., 2000). It contains a sea-ice model using a simple thermodynamic scheme (Cattle and Crossley, 1995). Two versions of land surface schemes can be used with this version of HadCM3, MOSES I

and MOSES II (Met Office Surface Exchange Scheme), and the latter one is chosen in our simulations (Cox et al., 1999; Essery et al., 2001; Essery and Clark, 2003).

In the assessment of multi-model simulations of the modern climate in East Asia, HadCM3 has been shown to have good abilities to simulate both surface air temperature and seasonal precipitation in East Asia in comparison with several other models (Jiang et al., 2005). The same study also shows that HadCM3 can simulate consistent variation trends with proxy data. HadCM3 has also been used to simulate the climate of the past interglacials, such as the Holocene, the LIG and MIS-13 (Muri et al., 2013; Otto-Bliesner et al., 2013; Stone et al., 2013; Roberts et al., 2014; Shi et al., 2020). It has been demonstrated to be an adequate model for studying the EASM response to changes in insolation, CO₂ and ice sheets.

In order to have a comprehensive assessment of the performance of HadCM3 in simulating the present East Asia climate, we performed a Pre-Industrial (PI) simulation and compared it with the reanalysis data. In the PI simulation, the eccentricity, obliquity, and longitude of perihelion are set to 0.01676, 23.46° and 100.33°, respectively (Berger, 1978), and the concentrations of CO₂, CH₄, and N₂O are 284.3 ppmv, 808.2 ppbv, and 273.0 ppbv, respectively. The simulation was run for 630 years, and the climatology of the last 30 years is used for analysis. The version V3 of NOAA-CIRES-DOE Twentieth Century Reanalysis (20CR) data is used (Compo et al., 2011; Slivinski et al., 2019). The resolution is 1° × 1° (360 × 181 grid points). The simulated summer (June to August) temperature, precipitation, wind fields at 850 hPa and vertical velocity are compared with the corresponding reanalysis data between 1836 and 1865.

The summer temperature in North China and Northeast China is higher, while the Northwest Pacific is colder in HadCM3 than in the 20CR dataset (Fig. 1a), which causes a larger land-sea thermal contrast. The temperature in South China and subtropical areas are relatively close. HadCM3 reproduces well the spatial pattern of summer precipitation obtained from the 20CR dataset (Fig. 1b). In the northern part of the EASM domain and Northeast China, the precipitation is simulated well. Slightly more precipitation is simulated in South China and the South China Sea and slightly less precipitation in Northwest China. The precipitation differences between the model and the 20CR are more obvious in the surrounding seas (Bohai Sea, Yellow Sea, and the East China Sea), with much less precipitation in the 20CR. The summer wind at 850 hPa is also well reproduced in Southeast China (Fig. 1c). One of the most important features of the EASM, the south wind blowing from the ocean to the land is well captured. The differences in the wind field are obvious in the north Pacific, with a much higher wind speed in HadCM3. The summer vertical velocity (indicated by negative omega) is another important index in East Asia, which is also shown in Fig. 1d. The general spatial distribution is consistent in the reanalysis and simulation data, but the details are different. There are two downdraft centers in 40°–50° N in HadCM3, while the downdraft is more scattered across the mid-latitude areas in 20CR. The vertical velocity is higher in the South China Sea in HadCM3, which can explain why HadCM3 produces more precipitation here than in the reanalysis data. In general, HadCM3 can reproduce the spatial pattern of climate in most regions of East Asia and capture the basic characteristics of EASM, although there are some differences between the simulated and reanalysis maps. This may be partially attributed to that forcings used in HadCM3 PI simulation are not exactly the same as in reality.

2.2. Experiments setup and forcing

Two sets of snapshot simulations are performed with a time interval of 2 ka covering the entire MIS-5 period, i.e. 71 ka - 133 ka.

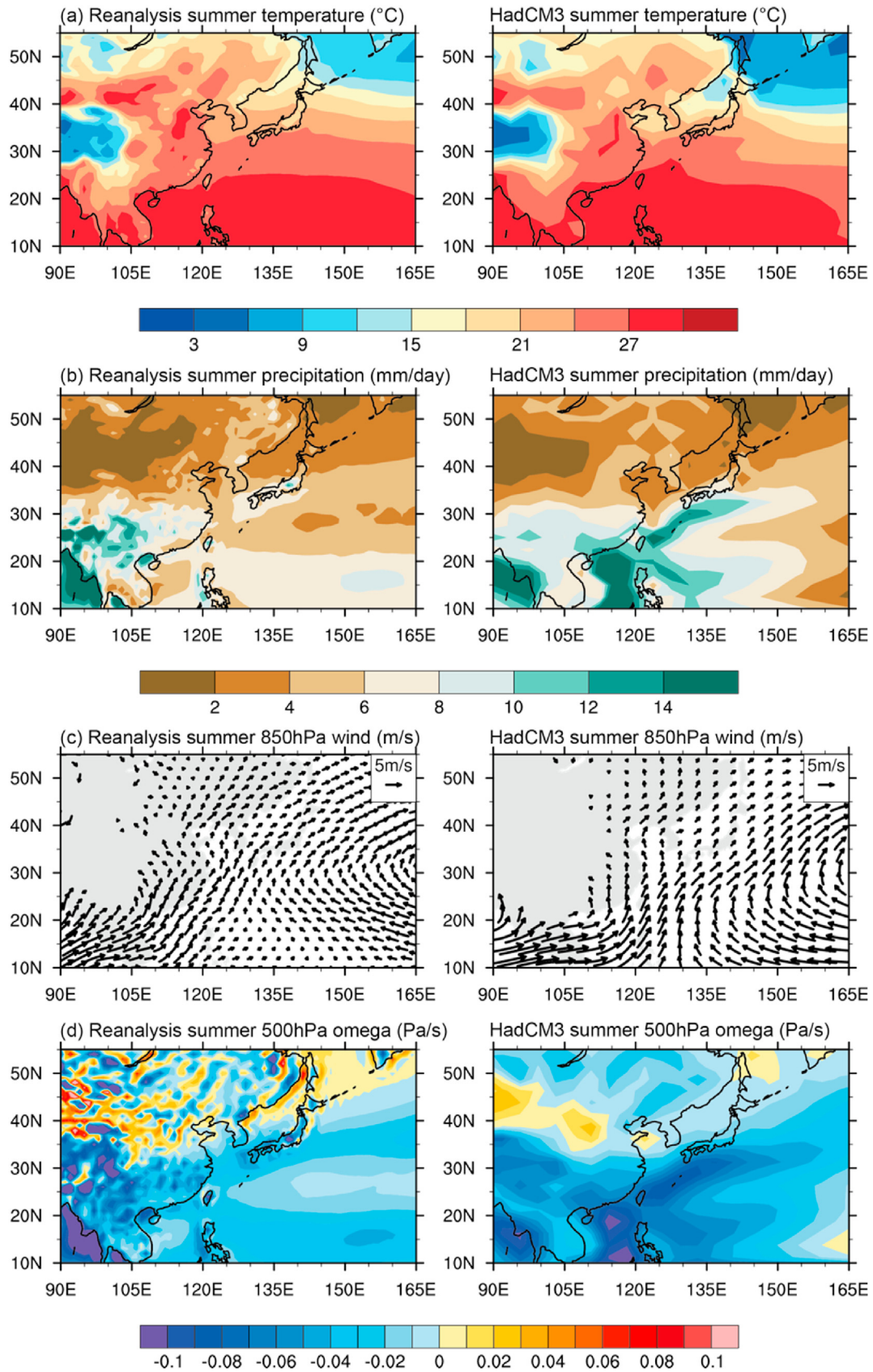


Fig. 1. Spatial distribution of (a) surface temperature (unit: °C), (b) precipitation (unit: mm/day), (c) wind at 850 hPa (unit: $\text{m}\cdot\text{s}^{-1}$), and (d) vertical velocity (indicated by omega, unit: $\text{Pa}\cdot\text{s}^{-1}$) at 500 hPa over East Asia in the boreal summer from reanalysis during 1836–1865 (left) and from HadCM3 during PI (right).

This leads to 32 experiments in each set of simulations and 64 in total for the two sets.

The first set (OrbGHG) is forced with the astronomical (Berger and Loutre, 1991) and Greenhouse gases (GHG) forcings. GHG mainly include CO₂ reconstructed from the Antarctica ice core (Lüthi et al., 2008), N₂O, and CH₄ (Loulergue et al., 2008; Schilt et al., 2010). The other boundary conditions are set as the PI values. The initial conditions of the OrbGHG simulations are the final state of the PI simulation. The OrbGHG experiments were run for at least 330 years and a quasi-equilibrium is reached in the surface climate. In the second set (OrbGHGIce), the ice sheet forcing is added, and the NH ice sheets simulated by Ganopolski and Calov (2011) are used. Starting from the final state of the OrbGHG experiments, the OrbGHGIce experiments run for another 200 years. In these experiments, the changes related to ice sheets include modifications of topography, surface type, vegetation parameters and soil properties. The topography is calculated by adding the simulated topography anomalies to the PI altitude in HadCM3. For the surface type, the fraction of ice is changed into 100%. The parameters related to the plant functional types, including leaf area index, canopy height, and canopy conductance are changed into their relative values obtained from the original grid box covered with ice. The soil properties (volumetric soil moisture concentration at critical, saturation, wilting points and at field capacity, Clapp-Hornberger B parameter, thermal conductivity of soil, saturated soil conductivity, thermal capacity of soil, saturated soil water suction, snow-free albedo and soil carbon content) are also changed into their relative values obtained from the original grid box covered with ice. The climatology of the last 30 years is used for analysis.

The values of astronomical parameters, GHGs and NH ice volume used at each simulated time slice are given in Fig. 2.

2.3. Moisture budget analysis

The atmospheric moisture budget analysis can be used to investigate the thermodynamic and dynamic contribution to precipitation changes (Held and Soden, 2006; Chou et al., 2009; Seager and Vecchi, 2010). Vertically integrated moisture budget analysis is used, and the moisture budget can be written as follows:

$$P = E + \delta - \langle \nabla \cdot \mathbf{v}q \rangle = E + \delta - \langle \omega \partial_p q \rangle - \langle \mathbf{v} \cdot \nabla q \rangle \quad (1)$$

where E is the evaporation at the surface, P is the precipitation, ω is the vertical velocity at a constant pressure coordinate, q is the specific humidity, and V is the horizontal winds. The angle brackets indicate the vertical integral over the atmospheric column throughout the troposphere (Chou and Lan, 2012). The convergence of moisture flux can be divided into two parts: the vertical moisture advection ($\langle \omega \partial_p q \rangle$) and the horizontal moisture advection ($\langle \mathbf{v} \cdot \nabla q \rangle$). The vertical moisture advection is the part of the convergence of moisture flux induced by vertical motion or low-level convergence. The horizontal moisture advection is the part of the convergence of moisture flux associated with horizontal velocity. The term δ is a residual term, which includes transient eddies and nonlinear effects.

The variations of moisture advection can be further decomposed into thermodynamic and dynamic components, which indicates the contribution to precipitation changes from changes in air water vapor content with unchanged circulation, and changes in horizontal or vertical motion with unchanged air water vapor content. ω is assumed to be zero at the surface and tropopause.

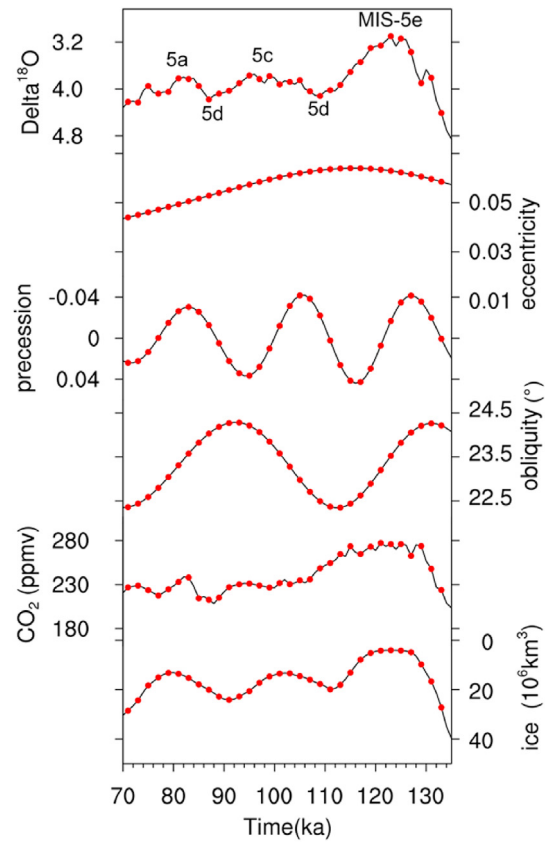


Fig. 2. Benthic $\delta^{18}\text{O}$ (‰) (Lisiecki and Raymo, 2005) during MIS-5 and the forcings used in the two sets of snapshot simulations, including the astronomical forcing (Berger and Loutre, 1991), CO₂ concentrations (Lüthi et al., 2008), and North Hemisphere ice volume (unit: 10^6 km^3) (Ganopolski and Calov, 2011). Red dots indicate the time slices of simulations performed for MIS-5. (For interpretation of the references to color in this figure legend, the reader is referred to the Web version of this article.)

$$- \langle \omega \partial_p q' \rangle = - \langle \overline{\omega \partial_p q'} \rangle - \langle \omega \partial_p \overline{q'} \rangle - \langle \omega' \partial_p q' \rangle \quad (2)$$

$$- \langle \mathbf{v} \cdot \nabla q' \rangle = - \langle \overline{\mathbf{v} \cdot \nabla q'} \rangle - \langle \mathbf{v}' \cdot \nabla \overline{q'} \rangle - \langle \mathbf{v}' \cdot \nabla q' \rangle \quad (3)$$

$$= - \langle \overline{u \partial_x Q'} \rangle - \langle \overline{v \partial_y Q'} \rangle - \langle u' \partial_x \overline{Q'} \rangle - \langle v' \partial_y \overline{Q'} \rangle - \langle u' \partial_x Q' \rangle - \langle v' \partial_y Q' \rangle \quad (4)$$

The prime denotes the differences between two experiments, and the overbar indicates the compared experiment. The first term in the right of (2) and (3) indicates the thermodynamic components of vertical and horizontal moisture advection, respectively. The second term in the right of (2) and (3) indicates the dynamic components. The third term in the right of (2) and (3) is non-linear terms. The horizontal moisture advection is decomposed along the zonal and meridional directions in (4).

3. Effect of astronomical forcing and CO₂ on climate during MIS-5

3.1. Relationship between astronomical forcing, CO₂ and climate during MIS-5

Previous studies using other model and emulator method show that astronomical parameters and CO₂ have different effects on different climate variables and in different regions during the past

800 ka not only at global scale but also in East Asia (Yin and Berger, 2012; Lyu et al., 2021). Therefore, we first quantify the relationship of the summer and mean annual temperature and precipitation with precession, obliquity and CO₂ during MIS-5 using the results of the first set of experiments for all the simulated time slices shown in Fig. 2, as the four climate variables could be most relevant to many paleoclimate records in East Asia. Multiple linear regression analysis was carried out to quantify the relative importance of these factors in different subregions in East Asia. The opposite value of precession (op_precession) instead of precession itself was used in the regression analysis because low precession corresponds to high summer insolation in the Northern Hemisphere, and vice versa. The CO₂ equivalent concentrations are calculated according to <https://gml.noaa.gov/aggi/aggi.html>.

For summer temperature, across East Asia, precession is the dominant influencing factor, followed by CO₂. Both op_precession and CO₂ have significant and positive effects. Obliquity has a weak effect in higher latitudes (north of 40° N) and has no statistically significant influence in the south of 40° N (Fig. 3). The situation is quite different for mean annual temperature (Fig. 3). CO₂ has a significant, positive effect on mean annual temperature across East Asia and is the dominant factor in mid-high latitudes of East Asia. Its effect is relatively weaker in East and Southwest China, Japan, and the surrounding ocean, i.e., the main EASM region. In these regions, precession is the dominant controlling factor on mean annual temperature. Obliquity is more important in the mid and high latitudes, which could be explained by the importance of obliquity on the annual irradiation in the mid and high latitudes (Berger et al., 2010). Compared to temperature, the response of precipitation to precession, obliquity and CO₂ is more spatially heterogeneous. For summer precipitation, precession plays an absolutely dominant role across East Asia. The correlation between op_precession and summer precipitation is positive in most of the EASM region and negative in Northeast China and North Pacific. By contrast, the influence of CO₂ and obliquity are quite limited, with relatively significant influence ($R^2 > 0.95$) only in Northwest and Southwest China, respectively. The significant influence by precession and minor impact by CO₂ and obliquity have been confirmed by a sensitivity study by Lyu et al. (2021). In the mean annual precipitation, although the effect of CO₂ is slightly increased in Southwest China and heavily increased in northeastern East Asia as compared to its effect on the summer precipitation, precession is still the major controlling factor for the precipitation in the EASM domain, due to the main contribution of summer precipitation to mean annual precipitation in monsoon regions.

The above analyses clearly show that precession, obliquity and CO₂ have different contributions on different climate variables. According to the diverse regional effect of these factors, East Asia is divided into several sub-regions and the temporal variations in summer and annual precipitation in each region are shown in Fig. 4.

The summer precipitation in the four sub-regions is high during the three interstadials (MIS-5a, MIS-5c, and MIS-5e), and low during the two stadials (MIS-5b and MIS-5d). In 30°–40° N, the two precipitation peaks at MIS-5c and MIS-5e are similar, due to similar precession values at these two substages and also due to insignificant influence of CO₂ on summer precipitation in most regions of northern China (Fig. 3). However, in 20°–30° N, the largest precipitation peak occurs at MIS-5e, which can be explained by the larger impact of CO₂ on summer precipitation in southern China and the higher CO₂ concentration at MIS-5e. Due to the main contribution from the summer precipitation, the variation of annual precipitation is similar to summer precipitation. The time of the highest mean annual precipitation is close to the time of the highest summer precipitation, which is during MIS-5e. The effect of CO₂ on annual precipitation is more obvious in southern China than

in the north, in line with the regression analysis shown in Fig. 3.

As far as summer temperature is concerned, the joint effect of precession and CO₂ can be more clearly seen than in summer precipitation. There are also three peaks in temperature which correspond to the three precession minima and the three substages MIS-5e, -5c and -5a. In the three sub-regions in the north, MIS-5e is the warmest and is obviously warmer than the other two peaks. In 20°–35° N, MIS-5e and -5c have similar warmth intensity, due to the joint effect of precession and CO₂. Interestingly, the variation of mean annual temperature is in anti-phase relationship with the variation of summer temperature, summer precipitation and mean annual precipitation, and each peak in the mean annual temperature corresponds to a precession maximum which means low summer insolation. This is because the mean annual temperature in East Asia is influenced more by winter temperature than by summer temperature (Fig. 5). Due to the dominant role of CO₂ in mean annual temperature (Fig. 3), there is a strong decreasing trend in mean annual temperature from early MIS-5 to late MIS-5 following the variation of CO₂.

3.2. Dynamics of the impact of insolation and CO₂ on temperature and precipitation

To have an in-depth understanding of the atmospheric and oceanic dynamics involved in the effects of insolation and CO₂, the results of four selected time slices are analyzed and compared. The simulated results at 115 ka and 129 ka are compared to investigate the effect of insolation, because the CO₂ concentrations are very similar between the two dates but insolation is very different. The results at 77 ka and 121 ka are compared to investigate the effect of CO₂ because of the very different CO₂ concentrations but similar insolation at the two dates (Fig. A1). During boreal summer, the Earth especially the NH receives much more insolation at 129 ka than at 115 ka with the maximum at the North Pole, and it receives less insolation in boreal winter with the minimum at low latitudes. This is a typical feature resulting from a large decrease in precession and a slight increase in obliquity. The CO₂ concentrations at 129 ka, 115 ka, 121 ka, and 77 ka are 273.75, 273.50, 277.27 and 217.56 ppmv, respectively. The NH summer insolation and CO₂ concentration of these four dates cover almost their maximum and minimum values during MIS-5. The comparison between them reflects therefore almost the largest effect of changes in insolation and CO₂ during MIS-5.

As expected from the change in insolation, it is much warmer in East Asia during boreal summer at 129 ka than at 115 ka and the warming is more pronounced towards the continent interior (larger than 5 °C) (Fig. 5a). At the same time, it is much colder in winter (December to February) (Fig. 5b). The change of mean annual temperature is more heterogeneous in space. It gets warmer in higher latitudes (North of 50° N), with a temperature of the ~1 °C but cooler in mid-low latitudes with a temperature decrease up to 2 °C (Fig. 5c), which is a typical feature due to a higher obliquity. The warming induced by a higher CO₂ is more homogeneous in space and season. It gets warmer in East Asia in both summer and winter at 121 ka than at 77 ka (Fig. 5d and e), and the warming is more pronounced in summer and towards the continental interior (up to 2 °C). Consequently, the mean annual temperature also increases by ~2 °C at 121 ka (Fig. 5f). The magnitude of seasonal temperature change caused by an increase of ~60 ppmv in CO₂ is much smaller than that caused by insolation, but it is similar for mean annual temperature.

As far as summer precipitation is concerned, the high summer insolation at 129 ka induces much more summer precipitation (larger than 30 mm/month) throughout the EASM region as compared to 115 ka (Fig. 6a), with the maximum increase occurring

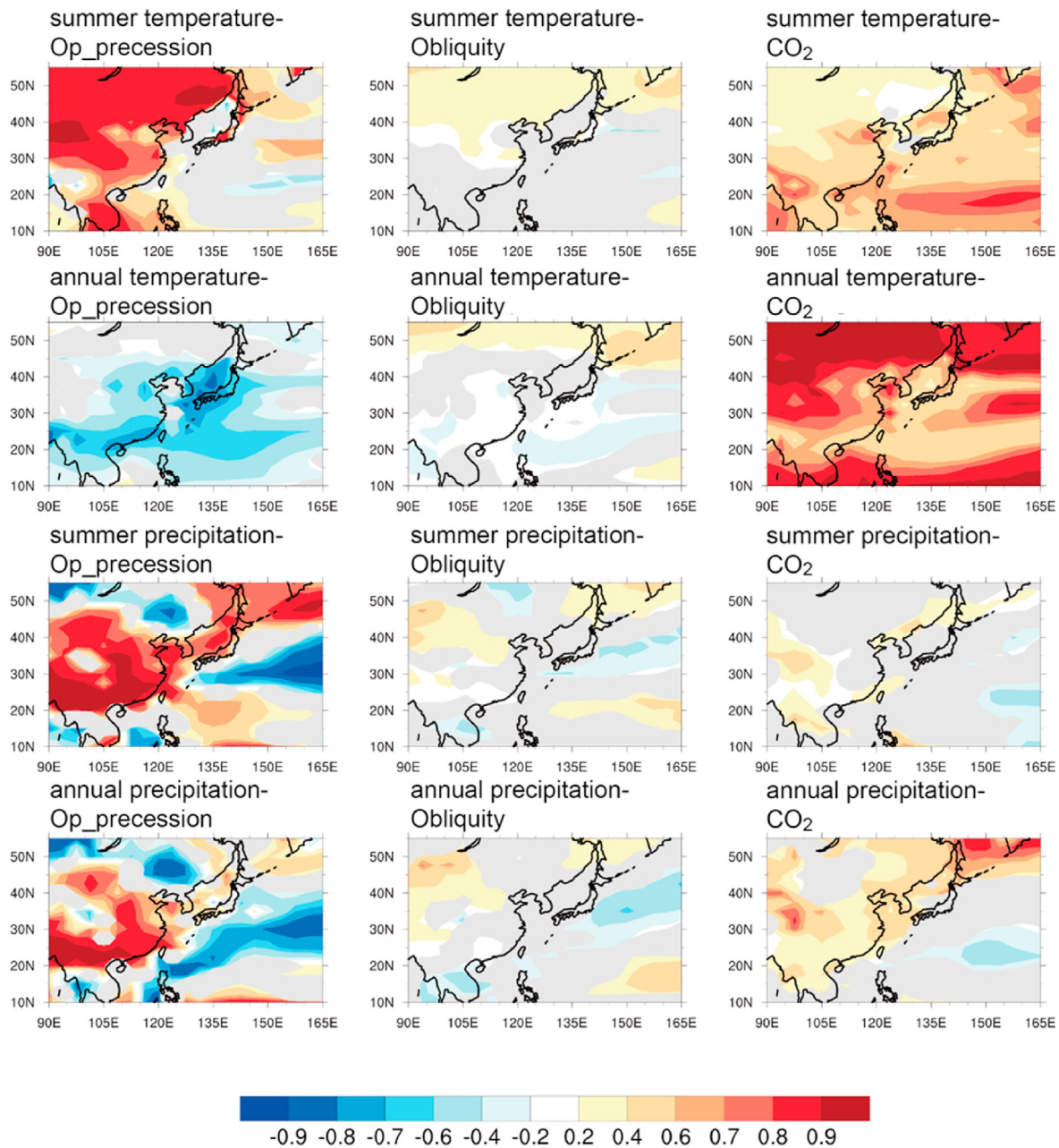


Fig. 3. Regression coefficients of multi-linear regressions between summer, annual temperature and precipitation (the predictands) and op_precession, obliquity and CO_{2eq} (the predictors). From the 1st to the 4th rows, it is for summer temperature, annual temperature, summer precipitation and annual precipitation, respectively; from the 1st to the 3rd columns, it is for the regression coefficients between these climate variables with op_precession, obliquity and CO_{2eq}, respectively. The multi-linear regressions were performed by using the results of the OrbGHG simulations of all the 32 time slices during MIS-5 after standardization. Regions where the respective coefficient is not statistically significant ($p > 0.05$) are grey shaded.

in South China and South China Sea (up to ~375 mm/month). The increase of CO₂ also leads to more precipitation in East Asia, but with a much smaller magnitude (up to ~68 mm/month) as compared with the effect of insolation (Fig. 6e). This is in agreement with the regression analysis presented in section 3.1, that insolation plays a more important role on summer precipitation in East Asia. Moisture budget analysis shows that the vertical dynamic component dominates the variations in the vertical moisture advection and summer precipitation during 129 ka (Fig. 6b). The vertical dynamic component is related to the vertical velocity of air mass. The meridional dynamic components also contribute to the positive anomaly of precipitation (not shown here). Different from the

effect of insolation, the thermodynamic components related to the temperature change in the air contribute more to the precipitation increase than the dynamic component in response to the CO₂ increase at 121 ka (Fig. 6f). The warmer air can hold more moisture content and lead to larger moisture flux convergence, contributing to increased rainfall.

To further understand the change in summer precipitation, the related processes are analyzed hereunder. In response to the high NH summer insolation at 129 ka, there is large warming (0.5–2.5 °C) on East Asia land and a slightly cooling (smaller than 1 °C) in the Western Pacific (Fig. 5a). This leads to a stronger land-sea thermal contrast and larger land-sea pressure contrast, which

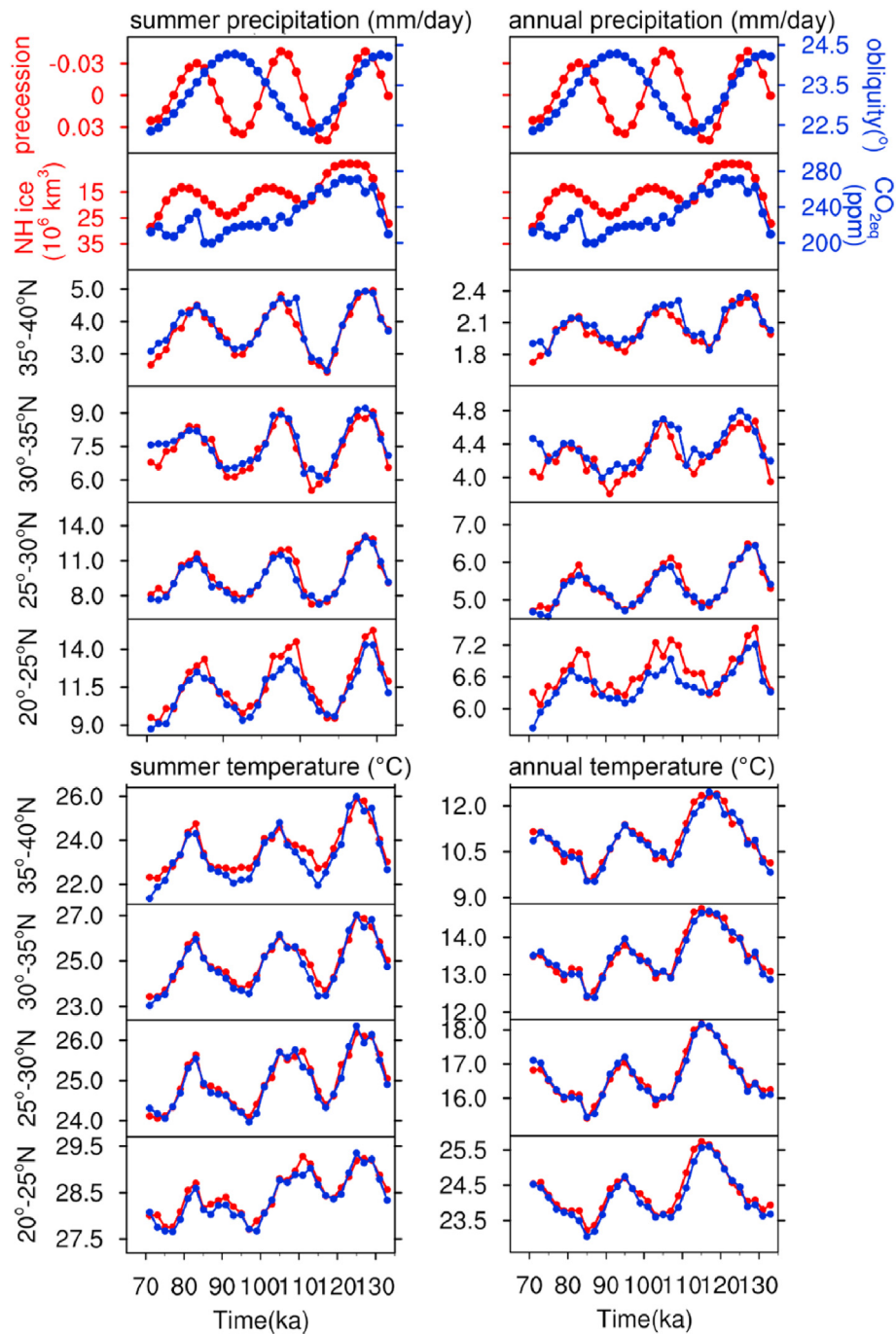


Fig. 4. Variations of precession, obliquity (Berger and Loutre, 1991), CO₂ (Lüthi et al., 2008) and NH ice sheets (Ganopolski and Calov, 2011), and simulated summer, annual precipitation (unit: mm/day) and temperature (unit: °C) in different sub-regions in East Asia. Dots indicate the time slices at which snapshot experiments were performed. Row 1 are for precession and obliquity respectively; in Row 2, they are for the NH ice volume and CO₂ concentration respectively; and in Rows 3 to 10, they indicate the results of OrbGHG and OrbGHGIce simulations, respectively.

favors a stronger EASM. This is confirmed by a strengthening of the southerly and southeasterly winds in East China and an anomalous high pressure in the Northwestern Pacific (Fig. 6c). The intensification of winds can bring more water vapor to South China, Southeast China and to North China. Fig. 6d shows the simulated summer vertical velocity anomalies (upward vertical velocity indicated by negative omega values) in pressure coordinates over East Asia (averaged between 105° E and 120° E). There is an upward anomaly of vertical velocity between 20° N and 40° N centered in 25° N, indicating a more intensified convection of air which causes

stronger water vapor convergence. In response to a CO₂ increase of ~60 ppmv, the land-sea thermal and pressure gradients between East Asia and the West northern Pacific slightly increase (Fig. 6g). As a consequence, the Southeasterly wind anomaly only exists along the eastern coastline in China and is not strong enough to reach further north and northwest into East Asian land, limiting the increase of precipitation. Although studies showed that an increase of CO₂ from 367 ppmv to its quadrupling 1468 ppmv could shift the location of the intertropical convergence zone (ITCZ) from 1° S to 0.75° N (Kug et al., 2021), the location of the ITCZ does not change

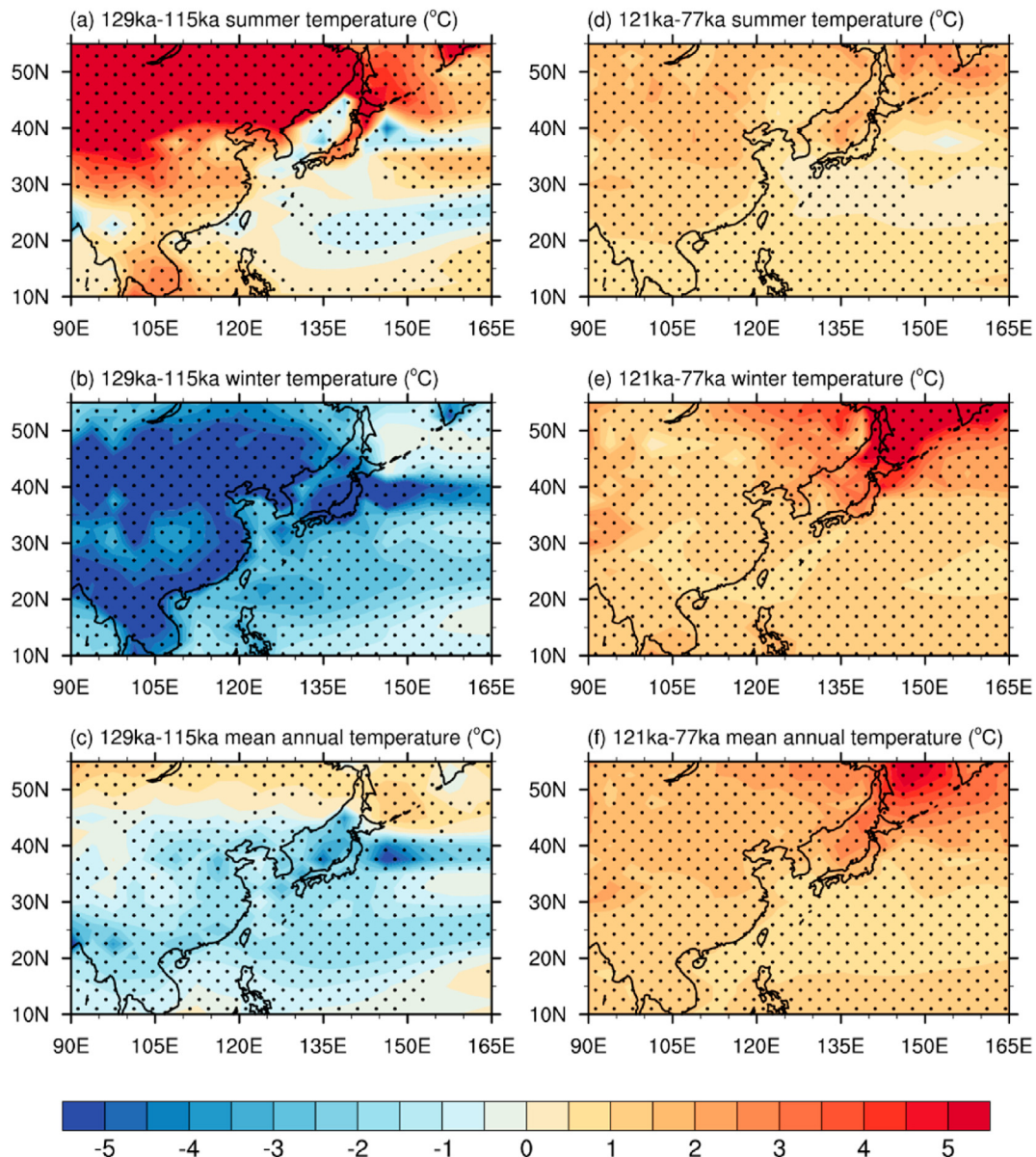


Fig. 5. Differences between 129 ka and 115 ka in (a) boreal summer (June to August), (b) winter (December to February), and (c) mean annual temperature (unit: °C). The black dots indicate that the differences are statistically significant at the 90% confidence level based on the Student's t-test. (d), (e) and (f) are same with (a), (b), and (c) but for differences between 121 ka and 77 ka.

obviously and there is no significant difference in the vertical movement of the air flow in response to a CO₂ increase of ~60 ppmv in our study (Fig. 6h).

4. Influence of NH ice sheets on the EASM climate

4.1. Temperature and precipitation changes response to ice sheet forcing

During the course of MIS-5, ice volume varies continuously, and the shape, area and location of ice sheets also vary. To analyze the impacts of ice sheets on the EASM climate, we will first examine the temporal variations of temperature and precipitation in response to ice sheet changes during the entire MIS-5 period. We will then investigate the spatial precipitation change induced by ice sheets and the related mechanisms by using the experiments at 115 ka, 79

ka and 73 ka which have different ice sheet attributes and background insolation (Fig. A2). 115 ka is at the early stage of the glacial inception and at this time, the North American ice sheet is quite flat with a large area but low height, and the Eurasian ice sheet is quite high. The NH summer insolation at 115 ka is lower than PI and is the lowest among the three time slices. At 79 ka, the ice sheets have a similar volume as at 115 ka (~32% of the LGM ice volume), but have different shape and size. The North American ice sheet has smaller area but is much higher, and the Eurasian ice sheet is negligible. The summer insolation at 79 ka is much higher than PI and 115 ka. At 73 ka, both the North American and Eurasian ice sheets have large area and are very high (~59% of the LGM ice volume) and the summer insolation is a bit higher than PI, but lower than 79 ka.

Fig. 4 shows the comparison between the OrbGHG and OrbGHGice experiments in the summer and annual temperature and precipitation in different subregions in East Asia. In general, the

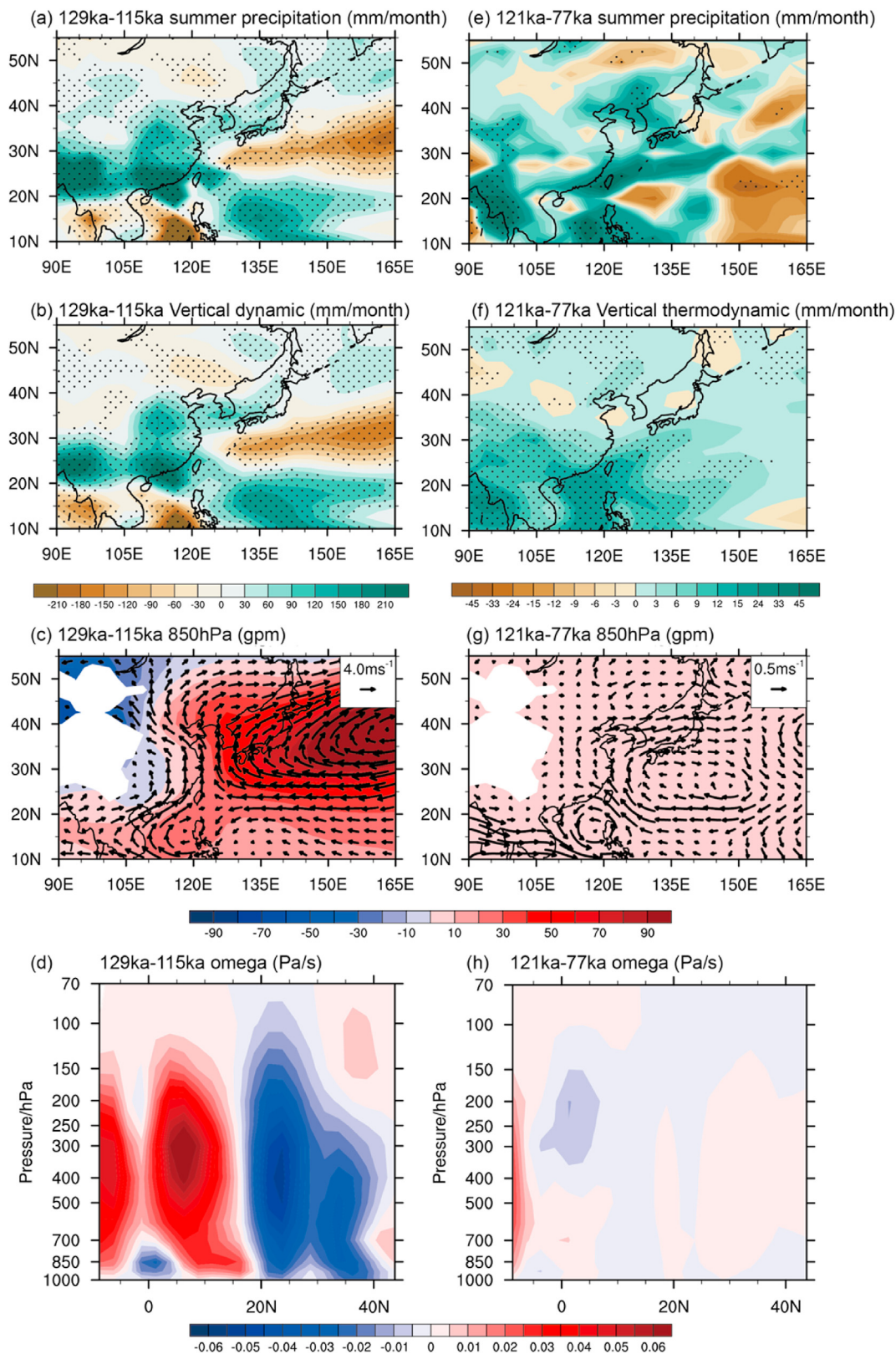


Fig. 6. Differences between 129 ka and 115 ka in summer (a) precipitation (unit: mm/month),(b) vertical dynamic term (unit: mm/month), (c) wind fields (arrows, units: $m \cdot s^{-1}$) and 850 hPa geopotential height (color shaded, unit: gpm), and (d) vertical velocity (indicated by Omega, in pressure coordinates over East Asia along 105° - 120° E, unit: $Pa \cdot s^{-1}$). The black dots indicate that the differences are statistically significant at the 90% confidence level based on the Student's t-test. (e), (f), (g) and (h) are same as (a), (b), (c), and (d) but for the differences between 121 ka and 77 ka. (For interpretation of the references to color in this figure legend, the reader is referred to the Web version of this article.)

differences between the two sets of experiments are very small in both temperature and precipitation, indicating the minor impact of ice sheets as compared with insolation. However, the impact of ice sheets on precipitation can still be clearly seen in some experiments. In the northern part of China, the summer and annual precipitation increase in most experiments in response to ice sheet volume increase, in particular around the three precession maxima at 117 ka, 95 ka and 71 ka. However, in the two southern subregions, the summer precipitation decreases in most OrbGHGce experiments, in particular at 127 ka, 105 ka and 83 ka (precession minima). It is also clear that the precipitation in 20° – 25° N is the most sensitive to ice sheet changes. Our previous finding based on emulator approach (Lyu et al., 2021) also shows ice sheets have large impact on the summer precipitation in southern China through their control on the latitudinal position of the ITCZ. As far as temperature is concerned, the impact of ice sheets is very small and almost negligible in both summer and annual temperature in the four subregions (Fig. 4) except an obvious cooling effect in the summer temperature in northern China when precession is around a maximum.

The small impact of ice sheets on the temperature in East Asia is quite surprising, because a strong cooling is usually expected in response to large ice sheets. To further investigate this problem, we plot the summer temperature changes at global scale in response to the large ice sheets (Fig. A2) at 73 ka. Fig. 7a shows that ice sheets induce strong cooling in the mid-high latitudes of both hemispheres, which is quite expected, and also induce strong warming over northern North Atlantic and eastern Europe, related to the ice sheet-induced wave pattern. However, the changes of summer temperature in East Asia are very small and are statistically insignificant (Fig. A3). To test the robustness of our results, the temperature changes in response to the ice sheets at 79 ka and 115 ka (Fig. 7b and c) are also investigated. At these two dates, the temperature changes over East Asia are also very small, insignificant except a significant summer cooling in northern East Asia at 115 ka.

4.2. Ice sheets-induced spatially heterogeneous monsoon and precipitation patterns over East Asia

In this section, summer precipitation changes induced by different ice sheet configurations are compared.

In response to the large ice sheets at 73 ka, the summer precipitation increases in a zonal band of $\sim 30^{\circ}$ – 40° N, but decreases to its north and south (Fig. 8a). This precipitation variation pattern results mainly from the change in the vertical dynamic component (Fig. 8b), and the horizontal dynamic term related to the meridional winds also contributes to the precipitation increase in 30° – 40° N (Fig. 8c). The 200 hPa geopotential height anomaly (Fig. 8d) shows that the introduction of ice sheets in the NH induces a strong negative anomaly in the NH mid-high latitudes. It also induces a strong wave pattern in the mid-latitudes, which is characterized by negative pressure anomalies over the North America ice sheet, the Europe-Mediterranean region, the northern Asian continent and positive anomalies in eastern China-southern Japan. Associated with this wave pattern, there are strong ascent (negative omega anomaly) in $\sim 30^{\circ}$ – 40° N and strong subsidence (positive omega anomaly) in the north of 40° N and in 20° – 30° N (Fig. 8f), which contribute to precipitation increase and decrease in the respective regions through the vertical dynamic effects. In addition to the vertical motion, the low-level land-ocean pressure gradient increases at 73 ka, and a strong anticyclone anomaly develops in the western Pacific (Fig. 8e). This leads to a southerly wind anomaly corresponding to the horizontal dynamic effect (Fig. 8e), which brings more moisture into East Asia explaining the precipitation increase in the meridional dynamic term (Fig. 8c).

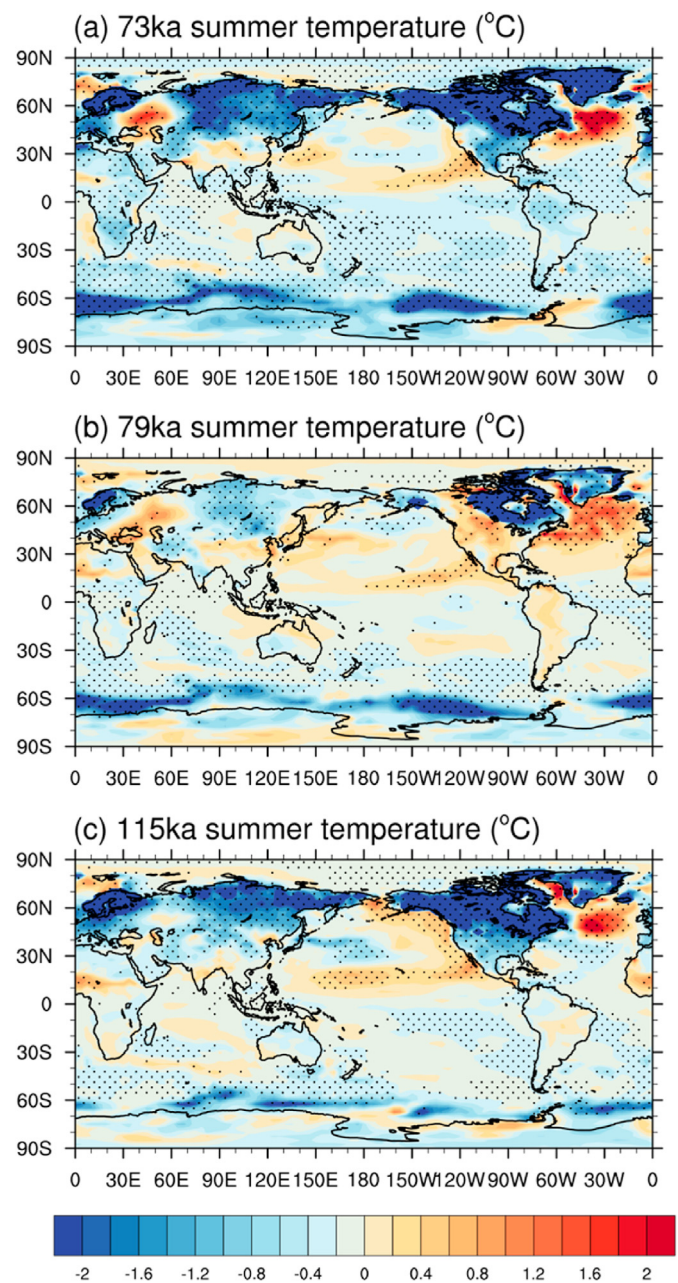


Fig. 7. Differences between OrbGHGce and OrbGHG experiments in summer temperature (unit: $^{\circ}$ C) at (a) 73 ka, (b) 79 ka, and (c) 115 ka. The black dots indicate that the differences are statistically significant at the 90% confidence level based on the Student's t-test.

Similar wave train patterns associated with the NH ice sheets have been observed in other modelling studies (Yin et al., 2008, 2009; Muri et al., 2012, 2013; Sundaram et al., 2012; Shi et al., 2020) despite different ice sheet configurations and different climate models. Yin et al. (2009) separated the individual roles of the North America and the Eurasian ice sheets and found that the Eurasian ice sheet alone could reinforce the summer precipitation in eastern China under the MIS-13 condition via topographically induced wave train. Such wave train has been confirmed to generate in barotropic or baroclinic atmospheres with topographic forcing (Grose and Hoskins, 1979). Our 73 ka experiment does not allow to investigate the individual effects of the two ice sheets, but the 79 ka experiment where the Eurasian ice sheets is almost negligible

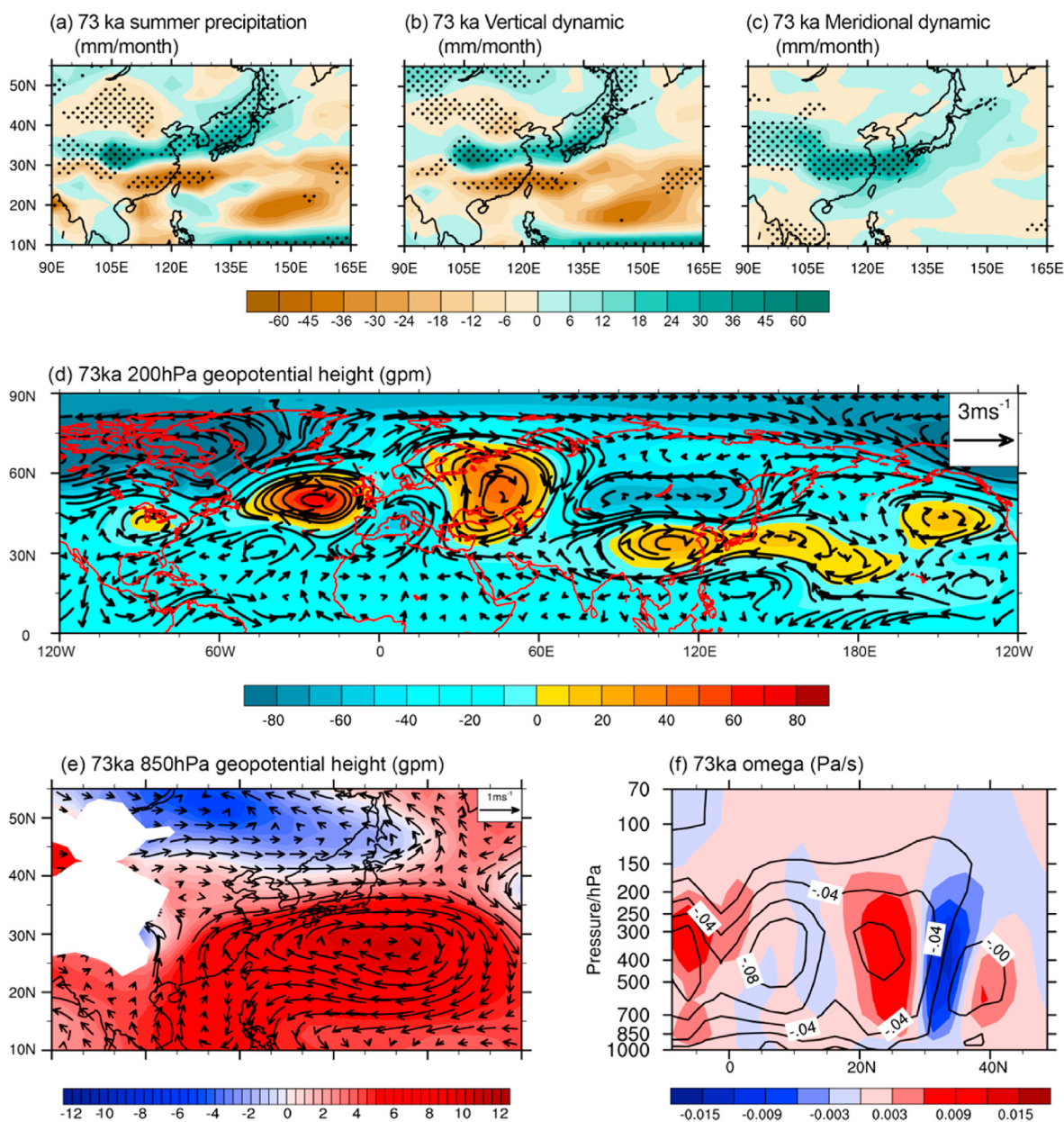


Fig. 8. Differences between OrbGHGIce and OrbGHG experiments at 73 ka in (a) summer precipitation (unit: mm/month), (b) vertical dynamic term (unit: mm/month), (c) meridional dynamic term (unit: mm/month), (d) 200 hPa wind fields (arrows, unit: $m \cdot s^{-1}$) and geopotential height (color shaded unit: gpm), (e) 850 hPa wind fields (arrows, unit: $m \cdot s^{-1}$) and geopotential height (color shaded, unit: gpm), and (f) vertical velocity (indicated by Omega, in pressure coordinates, the anomalies are shaded, and the results from OrbGHG are indicated by the contour lines, unit: $Pa \cdot s^{-1}$) over East Asia (105° – 120° E). The black dots indicate that the differences are statistically significant at the 90% confidence level based on the Student's t-test. (For interpretation of the references to color in this figure legend, the reader is referred to the Web version of this article.)

(Fig. A2) suggests that the North American ice sheet could also contribute to the wave pattern (see analysis below).

At 79 ka, as the Eurasian ice sheet is almost negligible (Fig. A2). The climatic changes could be regarded as caused mainly by the North American ice sheet, which is although significantly smaller than the one at 73 ka. Considering the different ice sheet and astronomical configurations, it is not surprising that the regional pattern of precipitation change in East Asia differs between the two dates. At 79 ka, the summer precipitation decreases in $\sim 20^{\circ}$ – 30° N but increases in its north and south (Fig. 9a). Similar to 73 ka, the precipitation change at 79 ka also results mainly from the vertical dynamic term (Fig. 9b), and the horizontal meridional dynamic term also contributes to precipitation increase in East Asia (Fig. 9c).

A similar wave pattern as at 73 ka is generated by the North American ice sheet at 79 ka, but the magnitude of positive and negative geopotential height anomalies is much weaker than the one at 73 ka (Fig. 9d) probably due to much smaller ice sheets and/or higher summer insolation. The positive geopotential height anomaly over East Asia is shifted more to the northeast at 79 ka and becomes also weaker. At the low level, there is an anticyclone anomaly over the western Pacific (Fig. 9e), which leads to stronger southerly and southeasterly wind and finally more precipitation in the meridional dynamic term (Fig. 9c). In the meantime, the subsidence at 20° – 30° N (Fig. 9f) could explain the precipitation decrease in this region, and the ascent to its north and south could explain the precipitation increase in these regions.

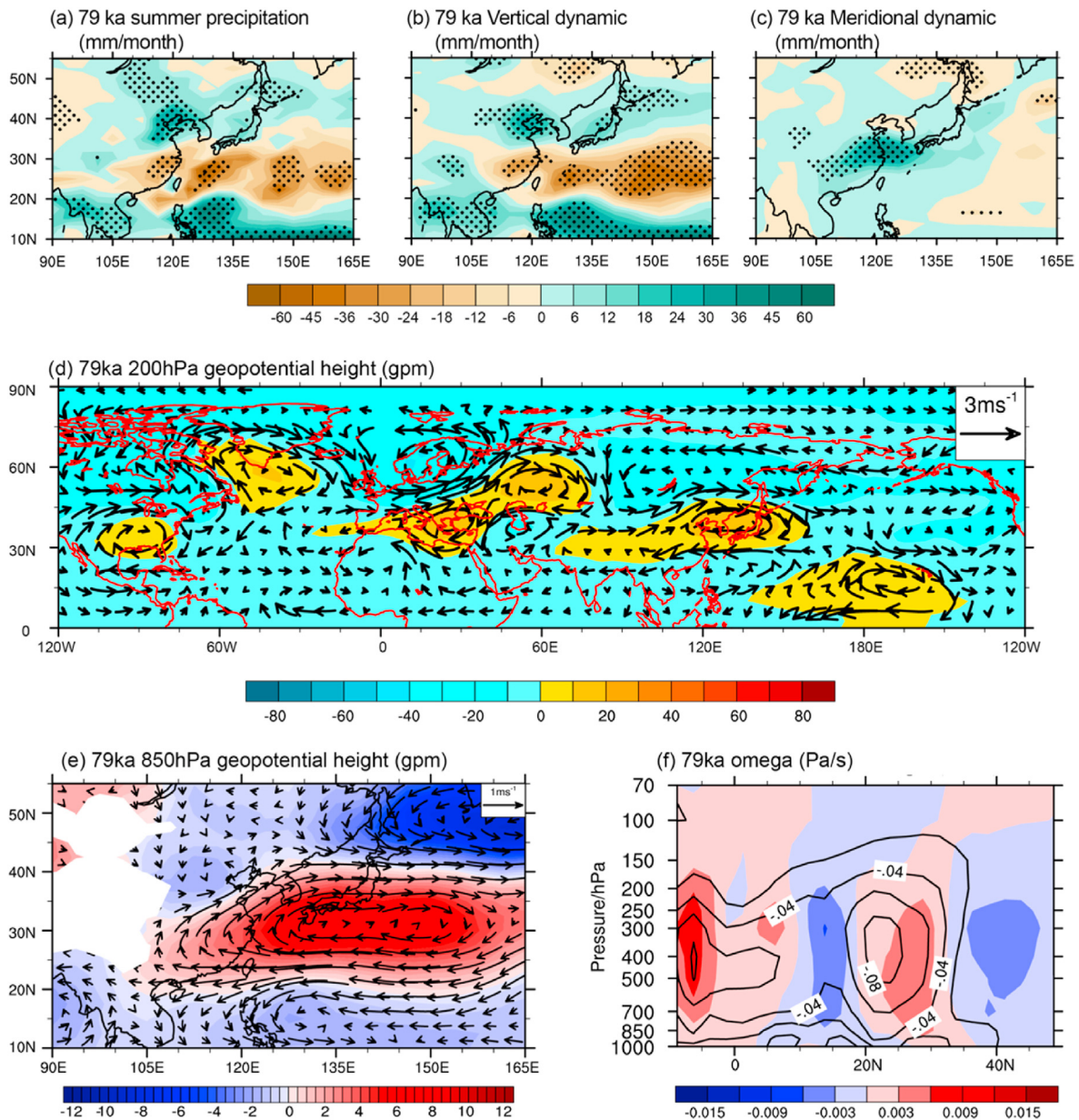


Fig. 9. Same as Fig. 8, but for 79 ka.

In response to the ice sheet configuration at 115 ka, the summer precipitation increases at $\sim 25^{\circ}$ – 35° N but decreases in most other parts (Fig. 10a). Again, the precipitation change pattern is mainly related to the change in the vertical dynamic component (Fig. 10b). As compared to 73 ka and 79 ka, what is particularly interesting is that the negative 200 hPa geopotential height anomaly in the mid-high latitudes at 115 ka is as strong as at 73 ka and much stronger than at 79 ka (Fig. 10d), but the wave pattern is much less pronounced at 115 ka than the other two dates. The area of the NH ice sheets at 115 ka is similar to the one at 73 ka (Fig. A2) and is much larger than the one at 79 ka. This implies that the negative 200 hPa geopotential height anomalies in the mid-high latitudes are caused by the cooling effect of the ice sheets due to increased albedo, while the wave pattern is more related to the ice sheet topography, in line with what has been found in Yin et al. (2009). The strong cooling effect but weak wave-train effect lead to a negative geopotential height anomaly at 850 hPa in western Pacific but a positive one over

China (Fig. 10e). Due to the reduced land-ocean pressure contrast, the EASM circulation weakens. The increase in precipitation over the middle and northern part of EASM region and decrease in other EASM regions are further influenced by the local vertical movement of air, indicated by the vertical velocity map (Fig. 10f).

5. Comparison between simulated MIS-5 climate with proxy records

In this section, selected geological records in East Asia are compared with the corresponding simulated climate during MIS-5 (Fig. 11). Fig. 11a shows the EASM index calculated from the OrbGHG and OrbGHGice experiments, respectively. The EASM index indicates the strength and variability of the Asian summer monsoon. It is defined as shear vorticity by Wang et al. (2008), $EASM\ index = U_{850}(110^{\circ}-140^{\circ}E, 22.5^{\circ}-32.5^{\circ}N) - U_{850}(90^{\circ}-130^{\circ}E, 5^{\circ}-15^{\circ}N)$, and U_{850} is JJA horizontal wind speed at 850 hPa. Figs. 11b–d

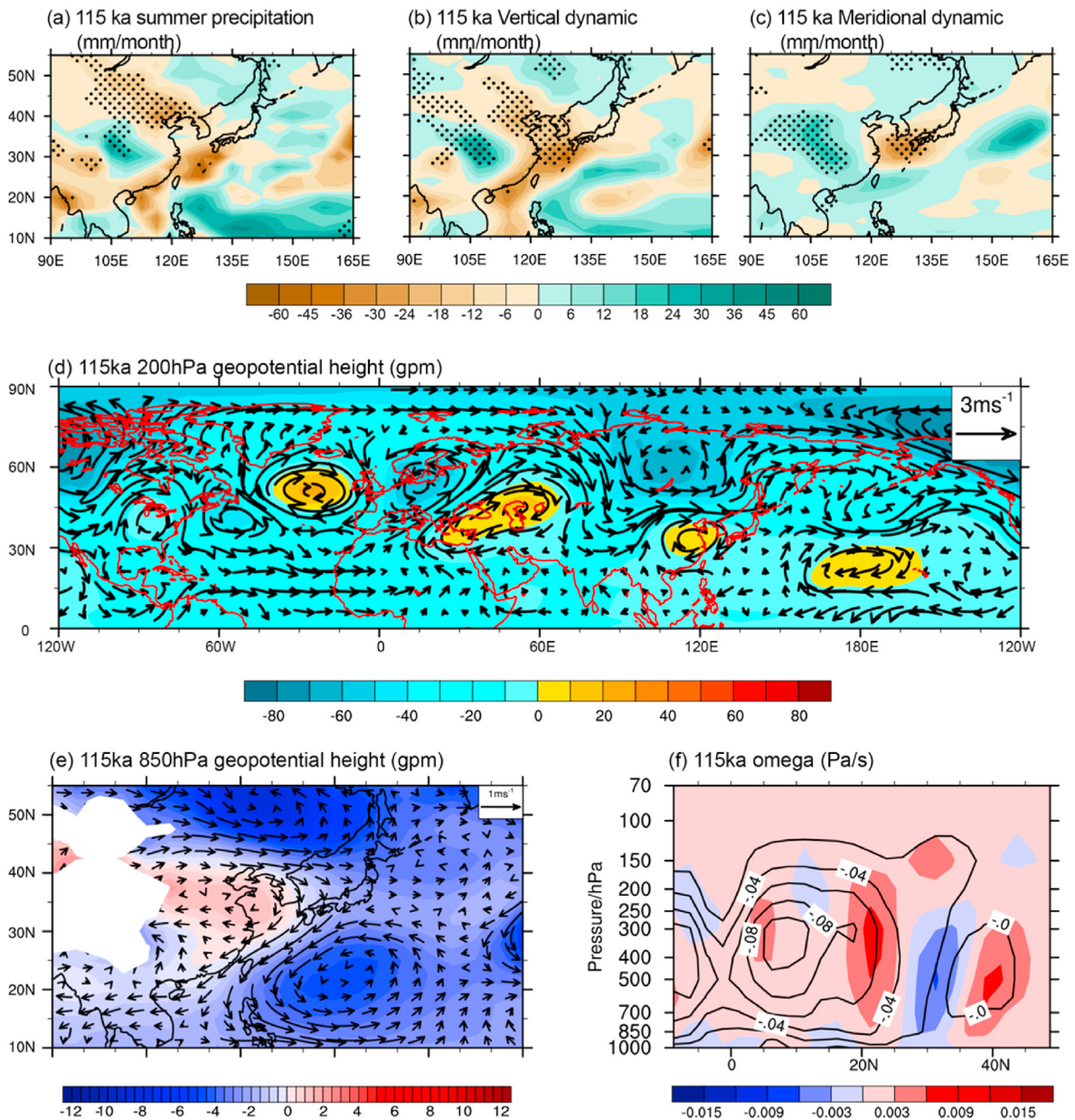


Fig. 10. Same as Fig. 8, but for 115 ka.

show the $\delta^{13}\text{C}$ record of loess carbonates from the Chinese Loess Plateau (CLP), the composite China speleothem $\delta^{18}\text{O}$ data and the stack of planktic $\delta^{18}\text{O}$ from the South China Sea, which can be regarded as the indicator for EASM intensity (Cheng et al., 2016; Wang et al., 2016; Sun et al., 2019). Three peak warmth and two cool stages are all presented in the three records and the simulated EASM index. The end of interglacial featured with the rapid cooling/drying is also captured in both the proxy data and the simulation results. However, MIS-5e is stronger than MIS-5c and MIS-5a in the loess and marine records, while there are no obvious differences among these substages in the speleothem and the simulation results. Fig. 11f shows the brGDGTs record from the CLP, which is suggested to reflect the temperature changes in the wettest months (Peterse et al., 2014). Fig. 11e shows the JJA temperature from the OrbGHG and OrbGHGIce experiments. In general, the simulated and proxy-based temperatures match well. Due to the limitation of

the depth, the peak warmth during MIS-5e is missing in the brGDGTs record. Fig. 11h shows the meteoric ^{10}Be from the CLP (MIS-5b and 5c are missing), which can be used as a proxy for annual rainfall (Beck et al., 2018). Fig. 11g shows the mean annual precipitation in 30°–35° N from the OrbGHG and OrbGHGIce experiments. The ^{10}Be -based precipitation reconstruction shows a significant increasing trend from 133 ka, peaking at 124.4 ka, and then decreasing. This is exhibited in the simulated annual precipitation in both the OrbGHG and OrbGHGIce experiments. The variation trend of the ^{10}Be during MIS-5a is more similar to the one from OrbGHG than OrbGHGIce.

In general, the simulation results match well with the selected proxy records. The model-data comparison for the MIS-5 further confirms the dominant role of precession on the EASM intensity and the reliability of the model results.

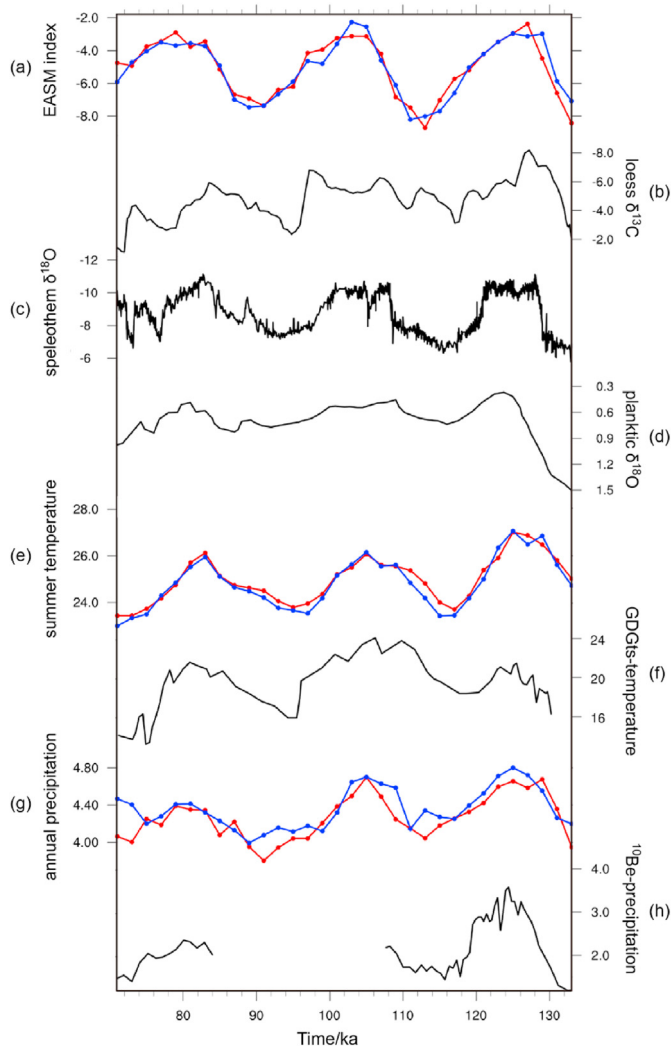


Fig. 11. (a) EASM index calculated from the OrbGHG (red) and OrbGHGIce (blue) experiments; (b) the $\delta^{13}\text{C}$ record of loess carbonates from the CLP (Sun et al., 2019); (c) composite China speleothem $\delta^{18}\text{O}$ data (Cheng et al., 2016); (d) the stack of planktic $\delta^{18}\text{O}$ from the South China Sea (Wang et al., 2016); (e) the simulated summer temperature (unit: $^{\circ}\text{C}$) in 30° – 35° N from the OrbGHG (red) and OrbGHGIce (blue) experiments; (f) the air temperature (unit: $^{\circ}\text{C}$) reconstructed by the GDDTs record from the CLP (Peterse et al., 2014); (g) the simulated mean annual precipitation (unit: mm/day) in 30° – 35° N from the OrbGHG (red) and OrbGHGIce (blue) experiments; and (h) the mean annual precipitation (unit: mm/day) reconstructed by the ^{10}Be record from the CLP (Beck et al., 2018). (For interpretation of the references to color in this figure legend, the reader is referred to the Web version of this article.)

6. Conclusions

To study the response of the climate in the EASM region to external forcing during the entire MIS-5, one set of snapshot experiments with astronomical and GHG forcing and the other one with astronomical, GHG and ice sheet forcing are performed with HadCM3. Moisture budget analysis is carried out to investigate the processes related to changes in summer precipitation.

Our results show that precipitation and temperature in different subregions in East Asia have different sensitivity to astronomical forcing, CO_2 and ice sheets, in particular when seasonal and mean annual changes are concerned. Precession plays a dominant role in summer precipitation, summer temperature and mean annual precipitation, while CO_2 has a larger effect on annual temperature. The variability of temperature and precipitation within MIS-5 is

therefore mainly controlled by precession with strongly pronounced sub-stages of MIS-5 which correspond to precession minima and maxima, but their magnitudes are modulated by CO_2 and ice sheets.

Insolation and CO_2 both have positive effect on the summer temperature and precipitation in East Asia. Within the range of its variations during MIS-5, the CO_2 concentration can cause similar degree of warming as insolation. However, the influence of CO_2 on precipitation is much weaker than the influence of insolation, and the relationship between summer precipitation and CO_2 is not statistically significant in most subregions in East Asia. Insolation and CO_2 affect the summer precipitation by the dynamic and thermodynamic processes, respectively.

Although ice sheets induce large cooling in the mid-high latitudes of both hemispheres, their impact on the precipitation and temperature in East Asia is quite small as compared to the impact of insolation. Their impact on summer precipitation in East Asia vary between regions and is also very sensitive to the area and height of the ice sheets and the background insolation. When local summer insolation is low, ice sheets reinforce the summer precipitation in northern China, while when insolation is high, ice sheets weaken the summer precipitation in southern China. The summer precipitation in southern China is more sensitive to ice sheets than in northern China. Ice sheets influence the EASM precipitation mainly through the vertical dynamic processes which is strongly associated with the ice sheet-induced wave train at the hemisphere scale.

Although our model results can capture most characteristics of the EASM during MIS-5 and match well some quantitative proxy reconstructions, limitations and potential uncertainties could still exist. For example, unlike the transient simulations, the snapshot simulations do not allow to investigate the transient response of the climate system to slow-varying forcing and therefore could underestimate the internal variabilities especially the centennial and millennial variabilities which could also play important role on the orbital-scale climate changes (e.g. Yin et al., 2021). Uncertainty may also arise from the unchanged sea level and land-sea distribution in our study. Given the large variations of ice volume during MIS-5, the land-sea distribution could have significantly varied. Model simulations show that the changes in land-sea distribution could have a strong effect on the EASM intensity (Zhang et al., 2007). Finally, in our study, only the changes of the NH ice sheets are considered and the Antarctica ice sheet is kept fixed to the present condition. Model simulations show that the changes of the Antarctica ice sheet could also affect the EASM (Shi et al., 2020). In the future, more comprehensive simulations could be carried out to reduce the uncertainties related to the various limitations.

Credit author statement

Anqi Lyu: Data curation, Investigation, Formal analysis, Methodology, Writing - Original Draft, Writing - Review & Editing, Validation, Visualization, Qiuzhen Yin: Conceptualization, Funding acquisition, Methodology, Supervision, Writing - Review & Editing.

Declaration of competing interest

The authors declare that they have no known competing financial interests or personal relationships that could have appeared to influence the work reported in this paper.

Data availability

Data will be made available on request.

Acknowledgements

This work is supported by the Fonds de la Recherche Scientifique-FNRS (F.R.S.-FNRS) under grant MIS F.4529.18. A. Lyu is supported by China Scholarship Council (CSC) Grant #201706190226. Q. Yin is Research Associate of F.R.S.-FNRS. Computational resources have been provided by the supercomputing facilities of the Université catholique de Louvain (CISM/UCL) and the Consortium des Équipements de Calcul Intensif en Fédération Wallonie Bruxelles (CÉCI) funded by the Fond de la Recherche Scientifique de Belgique (F.R.S.-FNRS) under convention 2.5020.11.

Appendix A. Supplementary data

Supplementary data to this article can be found online at <https://doi.org/10.1016/j.quascirev.2022.107689>.

References

- Beck, J.W., Zhou, W., Li, C., Wu, Z., White, L., Xian, F., Kong, X., An, Z., 2018. A 550,000-year record of East Asian monsoon rainfall from ^{10}Be in loess. *Science* 360, 877–881.
- Berger, A., 1978. Long-term variations of daily insolation and Quaternary climatic changes. *J. Atmos. Sci.* 35, 2362–2367.
- Berger, A., Loutre, M.-F., 1991. Insolation values for the climate of the last 10 million years. *Quat. Sci. Rev.* 10, 297–317.
- Berger, A., Loutre, M.-F., Yin, Q., 2010. Total irradiation during any time interval of the year using elliptic integrals. *Quat. Sci. Rev.* 29, 1968–1982.
- Cao, J., Wang, B., Liu, J., 2019. Attribution of the last glacial maximum climate formation. *Clim. Dynam.* 53, 1661–1679.
- CAPE-Last Interglacial Project Members, 2006. Last Interglacial Arctic warmth confirms polar amplification of climate change. *Quat. Sci. Rev.* 25, 1383–1400.
- Capron, E., Govin, A., Stone, E.J., Masson-Delmotte, V., Mulitza, S., Otto-Bliesner, B., Rasmussen, T.L., Sime, L.C., Waelbroeck, C., Wolff, E.W., 2014. Temporal and spatial structure of multi-millennial temperature changes at high latitudes during the Last Interglacial. *Quat. Sci. Rev.* 103, 116–133.
- Cattle, H., Crossley, J., 1995. Modelling Arctic climate change. *Philos. Trans. R. Soc. London, Ser. A: Phys. Eng. Sci.* 352, 201–213.
- Cheng, H., Edwards, R.L., Sinha, A., Spötl, C., Yi, L., Chen, S., Kelly, M., Kathayat, G., Wang, X., Li, X., 2016. The Asian monsoon over the past 640,000 years and ice age terminations. *Nature* 534, 640–646.
- Chou, C., Lan, C.-W., 2012. Changes in the annual range of precipitation under global warming. *J. Clim.* 25, 222–235.
- Chou, C., Neelin, J.D., Chen, C.-A., Tu, J.-Y., 2009. Evaluating the “rich-get-richer” mechanism in tropical precipitation change under global warming. *J. Clim.* 22, 1982–2005.
- Clark, P.U., Huybers, P., 2009. Interglacial and future sea level. *Nature* 462, 856–857.
- Compo, G.P., Whitaker, J.S., Sardeshmukh, P.D., Matsui, N., Allan, R.J., Yin, X., Gleason, B.E., Vose, R.S., Rutledge, G., Bessemoulin, P., 2011. The twentieth century reanalysis project. *Q. J. R. Meteorol. Soc.* 137, 1–28.
- Cox, P., Betts, R., Bunton, C., Essery, R., Rowntree, P., Smith, J., 1999. The impact of new land surface physics on the GCM simulation of climate and climate sensitivity. *Clim. Dynam.* 15, 183–203.
- Essery, R., Best, M., Cox, P., 2001. MOSES 2.2 Technical Documentation.
- Essery, R., Clark, D.B., 2003. Developments in the MOSES 2 land-surface model for PILPS 2e. *Global Planet. Change* 38, 161–164.
- Ganopolski, A., Calov, R., 2011. The role of orbital forcing, carbon dioxide and regolith in 100 kyr glacial cycles. *Clim. Past* 7, 1415–1425.
- Gao, Y., Liu, Z., Lu, Z., 2020. Dynamic effect of last glacial maximum ice sheet topography on the East Asian summer monsoon. *J. Clim.* 33, 6929–6944.
- Gordon, C., Cooper, C., Senior, C.A., Banks, H., Gregory, J.M., Johns, T.C., Mitchell, J.F., Wood, R.A., 2000. The simulation of SST, sea ice extents and ocean heat transports in a version of the Hadley Centre coupled model without flux adjustments. *Clim. Dynam.* 16, 147–168.
- Grose, W.L., Hoskins, B.J., 1979. On the influence of orography on large-scale atmospheric flow. *J. Atmos. Sci.* 36, 223–234.
- Held, I.M., Soden, B.J., 2006. Robust responses of the hydrological cycle to global warming. *J. Clim.* 19, 5686–5699.
- Herold, N., Yin, Q., Karami, M., Berger, A., 2012. Modelling the climatic diversity of the warm interglacials. *Quat. Sci. Rev.* 56, 126–141.
- Hu, C., Wang, Y., Li, A., Liao, J., Xie, S., 2015. Speleothem-based rainfall records: A comparison of the arid region of northwest China to the monsoon region of the eastern part of China. *Earth Sci. J. China Univ. Geosci.* 40, 268–274.
- Imbrie, J., Hays, J.D., Martinson, D.G., McIntyre, A., Mix, A.C., Morley, J.J., Pisias, N.G., Prell, W.L., Shackleton, N.J., 1984. The orbital theory of Pleistocene climate: support from a revised chronology of the marine $\delta^{18}\text{O}$ record. In: Berger, A., Imbrie, J., Hay, J., Kukla, G., Saltzman, B. (Eds.), *Milankovitch and Climate*. Reidel Publishing Company, Dordrecht, pp. 269–305.
- Jia, J., Xia, D., Wang, Y., Wang, B., Lu, H., Zhao, S., 2016. East Asian monsoon evolution during the Eemian, as recorded in the western Chinese Loess Plateau. *Quat. Int.* 399, 156–164.
- Jiang, D., Wang, H., Lang, X., 2005. Evaluation of East Asian climatology as simulated by seven coupled models. *Adv. Atmos. Sci.* 22, 479–495.
- Kug, J.-S., Oh, J.-H., An, S.-I., Yeh, S.-W., Min, S.-K., Son, S.-W., Kam, J., Ham, Y.-G., Shin, J., 2021. Hysteresis of the intertropical convergence zone to CO_2 forcing. *Nat. Clim. Change* 1–7.
- Landais, A., Masson-Delmotte, V., Capron, E., Langebroek, P.M., Bakker, P., Stone, E.J., Merz, N., Raible, C.C., Fischer, H., Orsi, A., 2016. How warm was Greenland during the last interglacial period? *Clim. Past* 12, 1933–1948.
- Lisiecki, L.E., Raymo, M.E., 2005. A Pliocene-Pleistocene stack of 57 globally distributed benthic $\delta^{18}\text{O}$ records. *Paleoceanography*.
- Li, X., Liu, X., Qiu, L., An, Z., Yin, Z.-Y., 2013. Transient simulation of orbital-scale precipitation variation in monsoonal East Asia and arid central Asia during the last 150 ka. *J. Geophys. Res. Atmos.* 118, 7481–7488.
- Loulergue, L., Schilt, A., Spahni, R., Masson-Delmotte, V., Blunier, T., Lemieux, B., Barnola, J.-M., Raynaud, D., Stocker, T.F., Chappellaz, J., 2008. Orbital and millennial-scale features of atmospheric CH_4 over the past 800,000 years. *Nature* 453, 383–386.
- Lu, Z., Liu, Z., Zhu, J., 2016. Abrupt intensification of ENSO forced by deglacial ice-sheet retreat in CCSM3. *Clim. Dynam.* 46, 1877–1891.
- Lüthi, D., Le Floch, M., Bereiter, B., Blunier, T., Barnola, J.-M., Siegenthaler, U., Raynaud, D., Jouzel, J., Fischer, H., Kawamura, K., 2008. High-resolution carbon dioxide concentration record 650,000–800,000 years before present. *Nature* 453, 379–382.
- Lyu, A., Yin, Q., Crucifix, M., Sun, Y., 2021. Diverse regional sensitivity of summer precipitation in east Asia to ice volume, CO_2 and astronomical forcing. *Geophys. Res. Lett.* 48, e2020GL092005.
- Masson-Delmotte, V., Schulz, M., Abe-Ouchi, A., Beer, J., Ganopolski, A., Rouco, J.G., Jansen, E., Lambeck, K., Luterbacher, J., Naish, T., 2013. Information from paleo-climate archives. In: Stocker, T.F., Qin, D., Plattner, G.-K., Tignor, M., Allen, S.K., Boschung, J., Nauels, A., Xia, Y., Bex, V., Midgley, P.M. (Eds.), *Climate Change 2013: the Physical Science Basis Contribution of Working Group I to the Fifth Assessment Report of the Intergovernmental Panel on Climate Change*. Cambridge University Press, Cambridge, pp. 383–464, 2013.
- Muri, H., Berger, A., Yin, Q., Karami, M.P., Barriat, P.-Y., 2013. The climate of the MIS-13 interglacial according to HadCM3. *J. Clim.* 26, 9696–9712.
- Muri, H., Berger, A., Yin, Q., Voldoire, A., Méliá, D.S.Y., Sundaram, S., 2012. SST and ice sheet impacts on the MIS-13 climate. *Clim. Dynam.* 39, 1739–1761.
- Nikolova, I., Yin, Q., Berger, A., Singh, U.K., Karami, M.P., 2013. The last interglacial (Eemian) climate simulated by LOVECLIM and CCSM3. *Clim. Past* 9, 1789–1806.
- Otto-Bliesner, B.L., Rosenbloom, N., Stone, E.J., McKay, N.P., Lunt, D.J., Brady, E.C., Overpeck, J.T., 2013. How warm was the last interglacial? New model–data comparisons. *Phil. Trans. Math. Phys. Eng. Sci.* 371, 20130097.
- Peterse, F., Martínez-García, A., Zhou, B., Beets, C.J., Prins, M.A., Zheng, H., Eglinton, T.I., 2014. Molecular records of continental air temperature and monsoon precipitation variability in East Asia spanning the past 130,000 years. *Quat. Sci. Rev.* 83, 76–82.
- Pope, V., Gallani, M., Rowntree, P., Stratton, R., 2000. The impact of new physical parametrizations in the Hadley Centre climate model: HadAM3. *Clim. Dynam.* 16, 123–146.
- Roberts, W.H., Battisti, D.S., Tudhope, A.W., 2014. ENSO in the mid-Holocene according to CSM and HadCM3. *J. Clim.* 27, 1223–1242.
- Schilt, A., Baumgartner, M., Blunier, T., Schwander, J., Spahni, R., Fischer, H., Stocker, T.F., 2010. Glacial–interglacial and millennial-scale variations in the atmospheric nitrous oxide concentration during the last 800,000 years. *Quat. Sci. Rev.* 29, 182–192.
- Seager, R., Vecchi, G.A., 2010. Greenhouse warming and the 21st century hydroclimate of southwestern North America. *Proc. Natl. Acad. Sci. USA* 107 (50), 21277–21282.
- Shi, F., Yin, Q., Nikolova, I., Berger, A., Ramstein, G., Guo, Z., 2020. Impacts of extremely asymmetrical polar ice sheets on the East Asian summer monsoon during the MIS-13 interglacial. *Quat. Sci. Rev.* 230, 106164.
- Shi, Z., Cai, Y., Liu, X., Sha, Y., 2018. Distinct responses of East Asian and Indian summer monsoons to astronomical insolation during Marine Isotope Stages 5c and 5e. *Palaeogeogr. Palaeoclimatol. Palaeoecol.* 510, 40–48.
- Slivinski, L.C., Compo, G.P., Whitaker, J.S., Sardeshmukh, P.D., Giese, B.S., McColl, C., Allan, R., Yin, X., Vose, R., Titchner, H., 2019. Towards a more reliable historical reanalysis: improvements for version 3 of the Twentieth Century Reanalysis system. *Q. J. R. Meteorol. Soc.* 145, 2876–2908.
- Stone, E., Lunt, D., Annan, J., Hargreaves, J., 2013. Quantification of the Greenland ice sheet contribution to Last Interglacial sea level rise. *Clim. Past* 9, 621–639.
- Sun, Y., Yin, Q., Crucifix, M., Clemens, S.C., Araya-Melo, P., Liu, W., Qiang, X., Liu, Q., Zhao, H., Liang, L., 2019. Diverse manifestations of the mid-Pleistocene climate transition. *Nat. Commun.* 10, 1–11.
- Sundaram, S., Yin, Q., Berger, A., Muri, H., 2012. Impact of ice sheet induced North Atlantic oscillation on East Asian summer monsoon during an interglacial 500,000 years ago. *Clim. Dynam.* 39, 1093–1105.
- Ullman, D.J., LeGrande, A.N., Carlson, A.E., Anslow, F.S., Licciardi, J.M., 2014. Assessing the impact of Laurentide Ice Sheet topography on glacial climate. *Clim. Past* 10, 487–507.
- Wang, B., Wu, Z., Li, J., Liu, J., Chang, C.-P., Ding, Y., Wu, G., 2008. How to measure the strength of the East Asian summer monsoon. *J. Clim.* 21, 4449–4463.
- Wang, P., Li, Q., Tian, J., He, J., Jian, Z., Ma, W., Dang, H., 2016. Monsoon influence on planktic $\delta^{18}\text{O}$ records from the South China Sea. *Quat. Sci. Rev.* 142, 26–39.

- Xue, G., Cai, Y., Ma, L., Cheng, X., Cheng, H., Edwards, R.L., Li, D., Tan, L., 2019. A new speleothem record of the penultimate deglacial: insights into spatial variability and centennial-scale instabilities of East Asian monsoon. *Quat. Sci. Rev.* 210, 113–124.
- Yao, T., Thompson, L., Shi, Y., Qin, D., Jiao, K., Yang, Z., Tian, L., Thompson, E., 1997. Climate variation since the Last Interglaciation recorded in the Guliya ice core. *Sci. China Earth Sci.* 40, 662–668.
- Yin, Q., Berger, A., Crucifix, M., 2009. Individual and combined effects of ice sheets and precession on MIS-13 climate. *Clim. Past* 5, 229–243.
- Yin, Q., Berger, A., Driesschaert, E., Goosse, H., Loutre, M.-F., Crucifix, M., 2008. The Eurasian ice sheet reinforces the East Asian summer monsoon during the interglacial 500 000 years ago. *Clim. Past* 4, 79–90.
- Yin, Q., Wu, Z., Berger, A., Goosse, H., Hodell, D., 2021. Insolation triggered abrupt weakening of Atlantic circulation at the end of interglacials. *Science* 373, 1035–1040.
- Yin, Q.Z., Berger, A., 2012. Individual contribution of insolation and CO₂ to the interglacial climates of the past 800,000 years. *Clim. Dynam.* 38, 709–724.
- Zhang, Z., Wang, H., Guo, Z., Jiang, D., 2007. What triggers the transition of palaeoenvironmental patterns in China, the Tibetan Plateau uplift or the Paratethys Sea retreat? *Palaeogeogr. Palaeoclimatol. Palaeoecol.* 245, 317–331.